Supporting Information for "Crystal fractionation by crystal-driven convection "

Cansu Culha[1]*, Jenny Suckale[1], Tobias Keller [2], Zhipeng Qin [1]

[1]Stanford University, Department of Geophysics, 397 Panama Mall, Stanford CA 94305, USA.
[2]University of Glasgow, School of Earth and Geographical Sciences, 8NN University Avenue, Glasgow G12 8QQ, UK.

Contents of this file

1. Text Sec. 1 to Sec. 7
2. Supp. Figures 1 to S6
3. Supp. Tables S1 to S2

Additional Supporting Information (Files uploaded separately)

1. Stokes Solver Fortran Code
2. Navier-Stokes Solver Fortran Code

Introduction

In this supplementary material we provide details regarding our nondimensional analysis and show additional simulation data. The codes are provided in our GitLab repository at this link: git@zapad.Stanford.EDU:cansu.culha/crystal-fractionation.git

In the manuscript and through out this supplementary material, we use a set of variables which are summarized in Table. 1 for the readers convenience. We note that all of the values presented in the manuscript are dimensionless, but here we differentiate dimensionless variables from dimensional by including $[\cdot]'$ to the variable, which is absent in the manuscript. We provide the methods section in Supp. Sec. 1, which includes the caveats of non-dimensionalization of our results and of using 2D experiments to describe 3D processes. A summary of all of all of the simulations are shown in Supp Table 2. Additionally, we explain how we calculate the cluster size (Supp. Sec. 2), the impact of the diffusive rim area on quantifying crystal segregation and fractionation (Supp. Sec. 3), the impact of domain size and initial randomness on cluster properties (Supp. Sec. 4), variability in efficiency (Supp. Sec. 5), and variability in crystal populations (Supp. Sec. 6).

1 Methods

To understand crystal fractionation in crystal-driven convection, we employ an idealized model setup where the upper boundary layer represents a cooling interface with negatively buoyant crystals suspended above a crystal-free melt body. We assume that the melt phase has constant density and viscosity, which means that the ensuing flow is entirely driven by the crystal-melt buoyancy contrast. Therefore, we are able to isolate crystal fractionation due to crystal-driven convection apart from other potentially confounding factors.

In the melt phase, we solve the incompressible Navier-Stokes equations,

*Stanford, CA, USA

Corresponding author: Cansu Culha, cculha@stanford.edu

Parameter	**Variable**
time	t
length	L
velocity	$\mathbf{v}$
pressure	P
gravity	g
force	F
location	X
mass	M
moment of inertia	I
angular momentum	ω
torque	T
viscosity	μ
density	ρ
segregation speed of 1 crystal	Δu
segregation speed	v_Δ
average segregation speed	$\overline{v_\Delta}$
cluster-melt segregation speed	V_Δ
av. spacing between crystals	l
crystallinity	ϕ
crystal radius	a
control area	A
area	Ω
crystal rich layer	Ω_T
volume	Ψ
crystal rich layer	Ψ_T
cluster size	R
Reynolds number	Re
Froude number	Fr
particle distribution	B
speed correction	$n = 1.8$
horizontal direction	$[\cdot]_x$
vertical direction	$[\cdot]_y$
of crystal	$[\cdot]_c$
of melt	$[\cdot]_\ell$
of cluster	$[\cdot]_d$
of tracers	$[\cdot]_t$
measured in simulation	$[\cdot]_m$
modeled	$[\cdot]_s$
mixture of crystal and melt	$[\cdot]_{cl}$
dimensionless $^+$	$[\cdot]'^+$

Table 1. $^+$ only applies for supplementary material

$$\nabla \cdot \mathbf{v}'_\ell = 0 \tag{1}$$

$$\mathrm{Re}\frac{\mathrm{D}\mathbf{v}'_\ell}{\mathrm{D}t'} = -\nabla P' + \nabla^2 \mathbf{v}'_\ell + \frac{1}{\mathrm{Fr}}\hat{\mathbf{y}}' + \mathbf{F}'_c \tag{2}$$

where $\mathbf{v}'_\ell$ is the non-dimensional velocity of the liquid, P' is the local non-dimensional pressure field, $\hat{\mathbf{y}}'$ is the unit vector parallel to gravity, and t' is non-dimensional time. F'_c is the non-dimensional force exerted by the crystals on the liquid. $\frac{D}{Dt'} = \frac{\partial}{\partial t'} + \mathbf{v}'_\ell \cdot \nabla$ is the material derivative. We assume that the melt is Newtonian and the non-linear interactions result from the presence of crystals. We describe the crystals as rigid bodies and they obey Newton's laws. For further detail on the approach, benchmarks for low Re number and high Re number, see Qin & Suckale (2017); Qin et al. (2019).

In order to isolate the mechanical aspect of crystal fractionation, all simulations are isothermal and isochemical, and we neglect crystal nucleation, growth, and dissolution. Throughout each simulation, we maintain a constant number of crystals in the domain. The simulations are performed on a 2D domain tens to hundreds of crystal radii wide, and with free-slip boundary conditions on the walls. The parameters for all simulations performed are summarized in Supplementary Table 1 and a summary of the non-dimensionalization relations are summarized in Supp. Sec. 2.

We assume that particles are rigid bodies and each crystal obeys Newton's laws:

$$M_c \frac{d\mathbf{V}_c}{dt} = \widetilde{\mathbf{F}}_c + M_c \mathbf{g} \tag{3}$$

$$\frac{d\left(\mathbf{I}_c \cdot \omega_c\right)}{dt} = \mathbf{T}_c \tag{4}$$

$$\frac{d\mathbf{X}_c}{dt} = \mathbf{V}_c \tag{5}$$

where c defines an individual crystal, M_c is the mass of an individual crystal, $\mathbf{V}_c$ is the crystal velocity at center of mass, X_c is the position at center of mass, $\mathbf{I}_c$ is the particle's moment of inertia tensor, and ω_c is the angular velocity of the crystal. $\widetilde{\mathbf{F}}_c$ and $\mathbf{T}_c$ are the hydrodynamic force and torque resulting from the surrounding fluid.

1.1 Nondimensionalization

We introduce dimensionless numbers to characterize the basic physical scales in the problem and present results in that framework for ease of comparison. In this section, we explain how we introduce a correction factor, n, to address the discrepancy in using 3D parameters to non-dimensionalize 2D simulation results. We describe the Stokes speed of a single crystal as the crystal-melt segregation speed and use it as the characteristic speed in our particle Reynolds number, Re. We model the Stokes settling speed as $\frac{2(\rho_c-\rho_\ell)ga^2}{9\mu}$ and hence define the crystal-melt segregation speed as

$$\Delta u_s = \frac{2(\rho_c - \rho_\ell)ga^2}{9\mu} \ , \tag{6}$$

where ρ_c and ρ_ℓ are crystal and liquid densities, a is crystal radius, and μ the liquid viscosity. This expression for the Stokes speed assumes a 3D flow field, but our simulations are only 2D. Ignoring this inconsistency would lead to a misrepresentation of Re. We hence re-scale the crystal-melt segregation speed, Δu, by our simulation results. We model a single crystal randomly placed in the domain and measure the segregation speed as described in the Manuscript v_Δ. We use the ratio of the stokes speed as shown in eq. 6 and our simulation speed of a single crystal to obtain a ratio, $\frac{\Delta u_s}{\Delta u_m} = n$ where Δu_m is the simulation result. The table below reports 3 simulations in $n = \frac{\Delta u_s}{\Delta u_m}$.

a[m]	μ**[Pa·s]**	Δu_s **eq. 6[m/s]**	Δu_m **stokes simulation[m/s]**	n
0.001	95	1.4488e-5	8.0692e-6	1.8
0.003	95	1.3039e-4	7.6076e-5	1.7
0.001	10	1.3764e-4	6.3561e-5	2.2

For simplicity, we scale all of our simulations by the same segregation speed correction factor and choose $n = 1.8$. Using this speed correction, we update our non-dimensional relationships,

$$L' = \frac{1}{a}L \tag{7a}$$

$$t' = \frac{\Delta u_m}{a}t = \frac{\Delta u_s}{na}t \tag{7b}$$

$$\mathbf{v}' = \frac{1}{\Delta u_m}\mathbf{v} = \frac{n}{\Delta u_s}\mathbf{v} \tag{7c}$$

$$P' = \frac{\Delta u_m}{\mu a}P = \frac{\Delta u_s}{n\mu a}P \tag{7d}$$

$$\mathrm{Re} = \frac{\rho_\ell \Delta u_m a}{\mu} = \frac{\rho_\ell \Delta u_s a}{n\mu} \tag{7e}$$

$$\mathrm{Fr} = \frac{\Delta u_m^2}{ag} = \frac{\Delta u_s^2}{agn^2} \tag{7f}$$

We use the non-dimensional number, B, to characterize the particle distribution. Our definition of B is $B = \frac{\phi a}{l}$, as stated in the paper, where l indicates the average crystal spacing,

$$l = \frac{(\Psi_T - N\frac{4}{3}\pi a^3)^{1/3}}{N} \tag{8}$$

$$= \frac{\Psi_c(\Psi_T(1-\phi))^{1/3}}{\Psi_T \phi} \tag{9}$$

where Ψ_T, Ψ_c, and N are the total crystal rich fluid volume, individual crystal volume, and the number of crystals, respectively for 3D and

$$l = \frac{(\Omega_T - N\pi a^2)^{1/2}}{N} \tag{10}$$

$$= \frac{\Omega_c(\Omega_T(1-\phi))^{1/2}}{\Omega_T \phi} \tag{11}$$

where Ω_T and Ω_c are the total crystal rich fluid area and individual crystal area, respectively for 2D .

Our numerical set up for all of the simulations is dimensional and keeps liquid and crystal density constant at 2360kg/m^3 and 3000 kg/m^3, respectively. Gravity is 9.8 m/s^2 for all of the simulations. We vary domain size, crystal size, viscosity, and crystal volume fraction to test different nondimensional regimes.

1.2 Implementing Passive Tracers

In order to track the liquid phase and identify the difference between residual melt and ambient melt, we add Lagrangian tracers into the domain. Unlike the crystals, which obey Newton's Laws of Rigid Body motion, tracers do not have mass and volume. They only track the flow field. These tracers are initially placed in a uniform spacing throughout the domain; then are randomly adjusted in space up to a distance that is half way between two tracers. By introducing a component of randomness, we hope

ϕ[%]	a[m]	μ[Pa·s]	l[m]	Re	B	$2R_m$ [m]	$2R'_m$	$\overline{v_{\Delta x}}$ [m/s]	$\overline{v_{\Delta y}}$ [m/s]	$V_{\Delta x}$ [m/s]	$V_{\Delta y}$ [m/s]	$\overline{v_{\Delta}}$ [m/s]	V_{Δ} [m/s]
5.0E-2	1.0E-3	95	1.4E-3	2.5E-7	3.7E-2	7.5E-3	7.5	1.0E-5	6.1E-6	9.8E-5	1.2E-4	8.0E-6	9.8E-5
5.0E-2	1.0E-3	95	1.4E-3	2.5E-7	3.7E-2	8.8E-3	8.8	9.2E-6	4.0E-6	2.6E-5	2.2E-5	6.5E-6	2.0E-5
5.0E-2	1.0E-3	95	1.4E-3	2.5E-7	3.7E-2	7.3E-3	7.3	9.7E-6	4.1E-6	6.8E-5	3.6E-5	6.8E-6	5.1E-5
5.0E-2	1.0E-3	1.0	1.4E-3	2.3E-3	3.7E-2	1.6E-2	16						
5.0E-2	1.0E-3	1.0	1.4E-3	2.3E-3	3.7E-2	9.7E-3	9.7	1.2E-3	4.0E-4	7.2E-3	3.5E-3	8.0E-4	5.3E-3
5.0E-2	2.0E-3	1.0E-1	5.5E-3	1.8	1.8E-2	7.5E-3	3.8	2.1E-2	8.2E-3			1.4E-2	
5.0E-2	2.0E-3	95	5.5E-3	2.0E-6	1.8E-2	1.9E-2	9.3	1.0E-4	3.4E-5	1.8E-4	6.0E-5	6.6E-5	1.1E-4
5.0E-2	2.5E-3	95	8.6E-3	4.0E-6	1.5E-2	1.4E-2	5.6	2.1E-4	4.5E-5	1.1E-4	4.7E-5	1.2E-4	7.1E-5
5.0E-2	2.5E-3	95	8.6E-3	4.0E-6	1.5E-2	1.3E-2	5.4	9.6E-5	2.3E-5	1.6E-4	5.4E-5	5.9E-5	1.0E-4
5.0E-2	2.5E-3	95	8.6E-3	4.0E-6	1.5E-2	1.4E-2	5.4	1.2E-4	2.5E-5	1.3E-4	5.7E-5	7.3E-5	9.5E-5
5.0E-2	2.5E-3	95	8.6E-3	4.0E-6	1.5E-2	1.4E-2	5.6	2.1E-4	4.5E-5	1.1E-4	4.7E-5	1.2E-4	7.1E-5
5.0E-2	4.5E-4	95	2.8E-4	2.3E-8	8.1E-2	1.1E-2	25	3.5E-6	1.6E-6	3.4E-5	3.0E-5	2.5E-6	3.2E-5
1.0E-1	1.0E-3	1.0E-1	6.7E-4	2.3E-1	1.5E-1	3.4E-3	3.4	2.4E-2	1.1E-2	3.9E-2	2.3E-2	1.7E-2	3.1E-2
1.0E-1	1.0E-3	1.0E-1	6.7E-4	2.3E-1	1.5E-1	6.3E-3	6.3	1.4E-2	7.5E-3	9.0E-2	9.2E-2	1.0E-2	8.2E-2
1.0E-1	1.0E-3	1.0E-2	6.7E-4	23	1.5E-1	7.9E-3	7.9	4.8E-3	3.2E-3	8.3E-3	5.1E-3	4.0E-3	6.7E-3
1.0E-1	1.0E-3	1.0E-2	6.7E-4	23	1.5E-1	3.2E-3	3.2	2.2E-2	9.6E-3	3.2E-2	8.5E-3	1.6E-2	2.0E-2
1.0E-1	1.0E-3	95	6.7E-4	2.5E-7	1.5E-1	1.6E-2	16	2.6E-5	1.7E-5	1.2E-4	8.6E-5	2.2E-5	1.0E-4
1.0E-1	1.0E-3	95	6.7E-4	2.5E-7	1.5E-1	2.1E-2	21	1.6E-5	9.0E-6	1.5E-4	1.5E-4	1.2E-5	1.5E-4
1.0E-1	1.0E-3	95	6.7E-4	2.5E-7	1.5E-1	1.4E-2	14	2.2E-5	1.4E-5	1.0E-4	8.2E-5	1.7E-5	9.1E-5
2.0E-1	1.0E-3	95	3.1E-4	2.5E-7	6.4E-1	1.6E-2	16	3.3E-5	2.6E-5	2.6E-4	2.1E-4	3.0E-5	2.3E-4
2.2E-1	1.0E-3	1.0	2.8E-4	2.3E-3	7.8E-1	8.2E-3	8.2	1.7E-3	1.1E-3	6.6E-3	3.7E-3	1.4E-3	5.0E-3
2.2E-1	1.0E-3	95	2.8E-4	2.5E-7	7.8E-1	1.9E-2	19	4.5E-5	2.5E-5	2.8E-4	1.6E-4	3.4E-5	2.0E-4
2.2E-1	2.0E-3	1.0E-1	1.1E-3	1.8	3.9E-1	8.3E-3	4.2	2.2E-2	1.3E-2	5.2E-2	2.6E-2	1.7E-2	3.2E-2
2.2E-1	1.0E-3	1.0E-2	2.8E-4	23	7.8E-1	5.2E-3	5.2	2.3E-2	1.1E-2	3.2E-2	1.5E-2	1.6E-2	2.1E-2
2.2E-1	2.0E-3	10	1.1E-3	1.8E-4	3.9E-1	2.3E-2	11	1.1E-4	6.9E-5	5.0E-4	2.1E-4	8.4E-5	3.3E-4
2.2E-1	2.0E-3	95	1.1E-3	2.0E-6	3.9E-1	2.5E-2	12	1.0E-4	4.8E-5	5.4E-4	2.1E-4	7.2E-5	3.6E-4
2.5E-1	1.0E-3	95	2.4E-4	2.5E-7	1.0	1.9E-2	19	5.1E-5	3.8E-5	2.3E-4	1.7E-4	4.3E-5	1.9E-4
2.5E-1	1.0E-3	95	2.4E-4	2.5E-7	1.0	2.7E-2	27	4.3E-5	3.3E-5	4.8E-4	2.9E-4	3.8E-5	3.7E-4
2.5E-1	1.0E-3	10	2.4E-4	2.3E-5	1.0	2.4E-2	24	2.3E-4	1.6E-4	1.9E-3	1.2E-3	1.9E-4	1.6E-3
1.0E-1	1.0E-3	95	6.7E-4	2.5E-7	1.5E-1	1.2E-2	12	1.6E-5	9.0E-6	5.5E-5	3.4E-5	1.2E-5	4.5E-5
1.0E-1	1.0E-3	95	6.7E-4	2.5E-7	1.5E-1	1.5E-2	15	2.4E-5	1.6E-5	2.8E-4	1.4E-4	1.9E-5	1.8E-4
1.0E-1	1.0E-3	95	6.7E-4	2.5E-7	1.5E-1	2.3E-2	23						

Table 2.

- CS-crystalline scale
- MS-mesoscale

to minimize the effects of tracer clustering and gap formation with time. At each time step, these tracers advect to a new location, $\mathbf{X}_t^{new}$ based on the liquid velocity interpolated to coincide with their original location, $\mathbf{X}_t^{old}$.

$$\mathbf{X}_t^{new} = \mathbf{X}_t^{old} + \mathbf{v_l} * dt \tag{12}$$

1.3 2D versus 3D

In summary, our set of results are conducted as 2D experiments, when the natural process is 3D. The general description of fractional crystallization is consistent between the dimensions. The formation of crystal-rich clusters during settling is consistent with analog experiments in 3D (Michioka & Sumita, 2005). Similarly, the crystal clusters come in different sizes and the crystal clusters sizes are independent of the domain size (Michioka & Sumita, 2005), which is a characteristic often associated with Rayleigh-Taylor Instability. However, quantifying the transition from 2D to 3D of the process is nontrivial. For example, 2D volume fraction of crystals is not the same as 3D volume fraction of crystals. Although we approximate a linear correction factor n, segregation speeds and, hence, the rate of crystal fractionation might not translate linearly. Therefore, these results should be taken to describe the general process. Crystal clusters at low to intermediate crystallinity dominate the terrestrial magmatic systems. They result in crystal fractionation that is more efficient than hindered settling but the efficiency decreases under certain conditions. Crystal clusters can lead to crystals sampling different melt environments. Depending on the dynamic nature of the crystals, neighboring crystals may have different compositional content and profiles.

2 Calculating cluster size

We want to be able to describe when crystals settle collectively versus individually. In order to identify whether crystals are in collective units, we look at the horizontal cross sectional size of the negative vertical velocity and compute a wavelength that is scaled by crystal size. In a crystal cluster, the center of mass of particles does not necessarily define the convective head. We therefore take a horizontal cross section at the crystal center of mass, at 0.1 domain lengths below and 0.1 domain lengths above the crystal center of mass. We collect the dominant widths for the entire time the particles are advecting in the center half of the domain. Then we average over all the widths that are greater than the crystal radius to compute $R'_m = R_m/a$. These values appear as filled circles in Fig. 1I of the Manuscript.

In order to generalize the system and depict the transition of individual to collective settling behavior, we developed a scaling relationship dependent on Re and B. As suggested by our cluster size measurements, the cluster size increases with increase in long range interactions, which is dependent on viscous forces (at low Re) and B. We hypothesize that the cluster formation occurs at the balance of particle speed, which is set by cluster speed, and speed at which long range interactions communicate. We identify the long range interaction speed as $\frac{\eta_{cl} B}{R}$, where $\eta = \frac{\mu}{\rho_{cl}}$ is the kinematic effective viscosity as a function of ϕ and R is the suitably defined size of the cluster. We generalize the Stokes settling speed to clusters to approximate cluster speed.

$$\Delta u_{sd} = \frac{2(\rho_{cl} - \rho_\ell) g R^2}{9\mu} \tag{13}$$

where ρ_{cl} is the mixture of the crystal and melt density, μ is the mixture viscosity which is dependent on crystallinity of the bottom melt and R is a suitably defined size of the cluster. We set the two speeds equal to one another,

$$\frac{\frac{\mu}{\rho_{cl}} B}{R} = \frac{2(\rho_{cl} - \rho_\ell) g R^2}{9n\mu} \tag{14}$$

solving for R, we obtain the dimensional form,

$$R = \left(n \frac{9\mu^2 B}{2\rho_{cl}\Delta\rho_{cl} g} \right)^{\frac{1}{3}} . \tag{15}$$

The plotted relationship in the Manuscript, Fig. 1, is the non-dimensionalized R,

$$R' = \frac{1}{a}\left(n \frac{9\mu^2 B}{2\rho_{cl}\Delta\rho_{cl} g} \right)^{\frac{1}{3}} . \tag{16}$$

This relationship approximates the pattern of decrease in cluster size with decrease in Re and B. We show the results from this analysis as the background color of Fig. 1I of the Manuscript.

3 Impact of the diffusive rim area on crystal segregation and fractionation

Our approach in measuring segregation speed and crystal fractionation uses a diffusive rim control area of radius A around the crystal. We test the sensitivity of A on crystal fractionation and crystal segregation in Supp. Fig. 1.

In Supp. Fig. 1A–B, we show that the choice of A uniformly alters the degree of fractionation. However, the non-linear effects of crystal-melt interactions result in a slight increase in segregation speed with increase in A for cluster-forming simulations (Supp. Fig. 1C–D). The A we use provides a lower segregation speed than the larger As we could have picked from such that we can be conservative with our findings.

4 Impact of domain size and initial randomness on cluster properties

Two immersible fluids that are unstably stratified in density was first proven to have a convective instability by Rayleigh (1883) and Sir Geoffrey (F.R.S.) (1950). The size of the diapiric instability depends on domain size. Since the introduction of Rayleigh-Taylor, many multiphase fluid systems were identified as an instability reminiscent of the original instability. Since our system also includes unstable density stratification, we test the dependence of cluster size on domain size. We find that our results are independent of domain size (Supp. Fig. 2). However, we do find that the randomness of the initial crystal placements results in variable number of clusters and variable cluster sizes as captured by Fig. 1I in the Manuscript. We provide 4 simulations to illustrate this variability in Supp. Fig. 3.

5 Efficiency of crystal fractionation is dependent on crystallinity

In the Manuscript, we notice that there is an increase in crystal-melt and cluster-melt segregation speed with increase in B. Our results show that at a constant Re, increasing B has a positive correlation with increase in segregation speeds. Supp. Fig. 4 summarizes this finding where we plot each of the simulations as a dark spot to indicate cluster-melt segregation and an open circle as crystal-melt segregation. Because the simulations are all at a constant Re, we only vary crystallinity in the top domain in these simulations. There are multiple segregation speeds for each B because each simulation had a different cluster form. The enhanced crystal-melt segregation speeds compared to single crystal stokes sinking speed may lead to comparable or higher crystal fractionation rates. The formation of the quickly sinking cluster forces the outer rim crystals to also quickly segregate from their surrounding melt compared to individually settling crystals.

However, the efficiency of crystal fractionation decreases with increasing overall crystallinity and removing the crystal gradient. We show the limits of crystal cluster

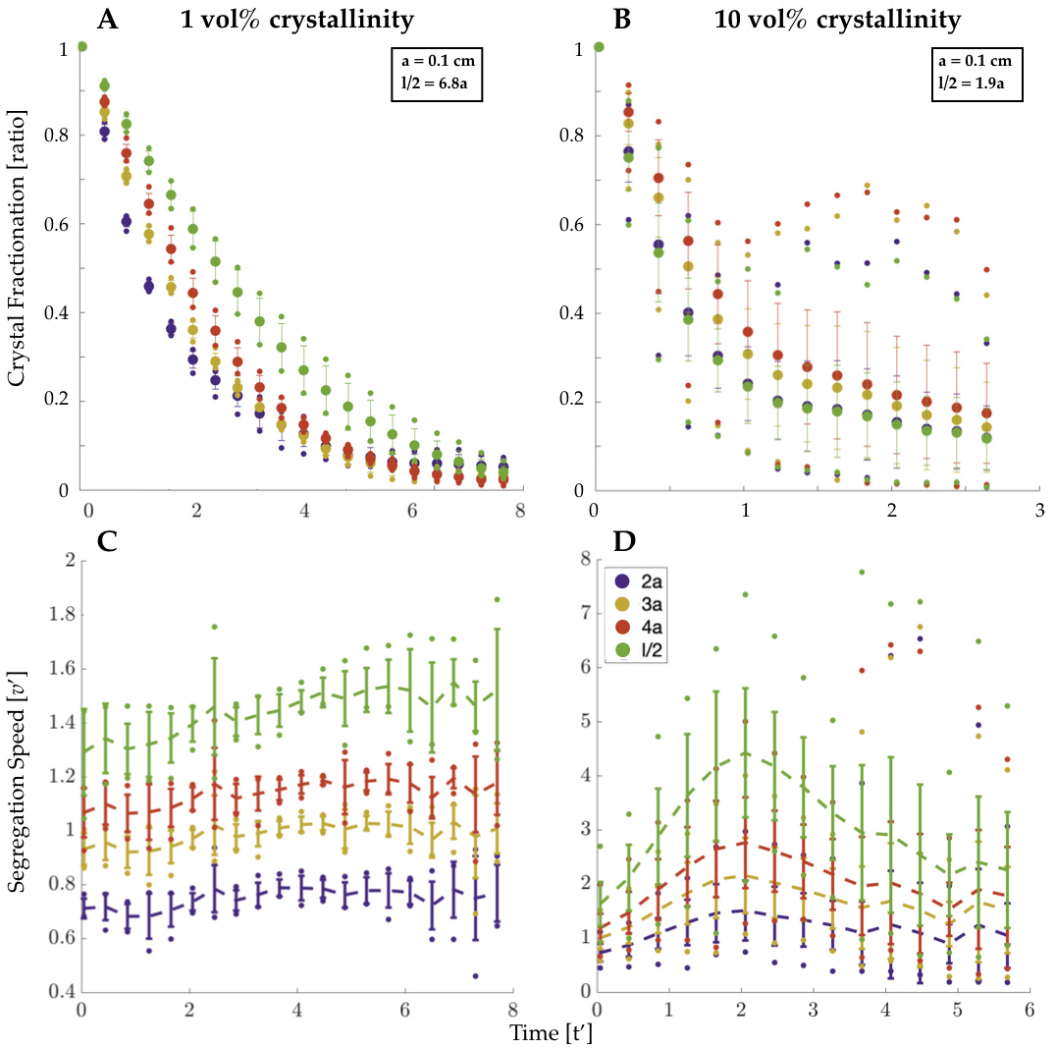

Figure 1. (A–B) The dependence of crystal fractionation on A as defined in the Manuscript. (C–D)The dependence of crystal-liquid segregation speed on A as defined in the Manuscript. (A& C) are for 1 vol% crystallinity whereas (B & are for 10 vol% crystallinity.

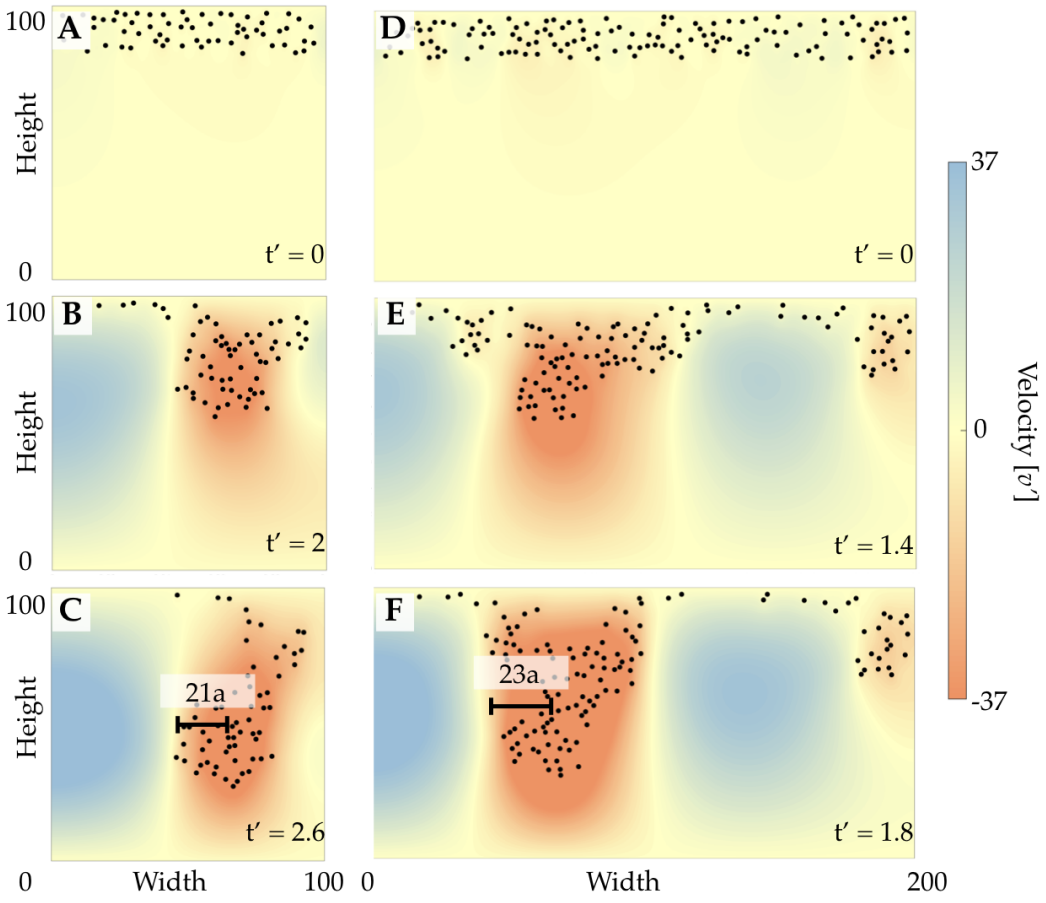

Figure 2. Testing sensitivity of cluster size, R', to width of the domain. These are both at 10 vol% crystallinity with same viscous liquid properties.

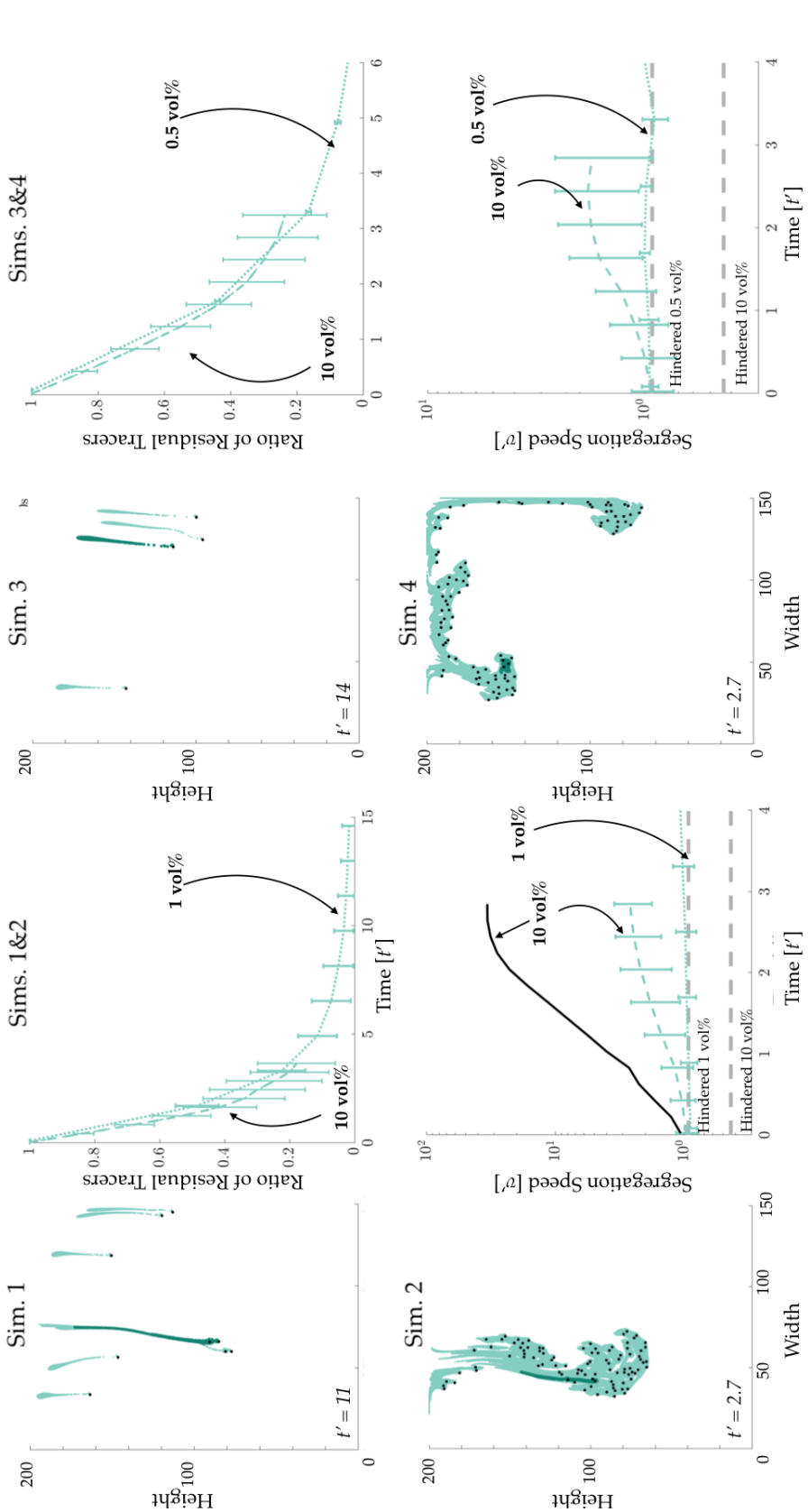

Figure 3. Extra simulation runs. The figure is set up to mimic Fig. 2 in the Manuscript. Simulation 1 and 3 are at 1 and 0.5 vol% crystallinity. Simulation 2 and 4 are at 10 vol% crystallinity. Simulation 2 is the same as Fig. 3 in the Manuscript. We show the segregation speeds and crystal fractionation rates Γ. We only show cluster-melt segregation speed for Simulation 2. Additionally, for figure simplicity, we do not show the individual crystal-melt segregation and crystal fractionation in dark turquoise.

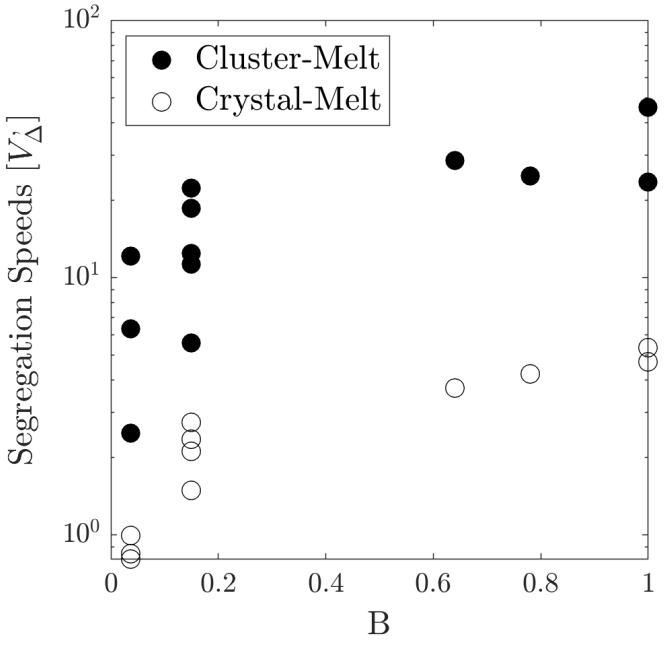

Figure 4. The variation in the average crystal segregation speed, $\overline{v_\Delta}$, and the cluster segregation speed, V_Δ with B.

fractionation in Supp. Fig. 5 for 10 vol% crystallinity gradient and 0 vol% crystallinity gradient. We compare 4 simulations, Sim. (1) with 10 vol% crystallinity on top and 0 vol% crystallinity on the bottom, Sim. (2) with 20 vol% crystallinity on top and 10 vol% crystallinity on the bottom, Sim. (3) with 30 vol% crystallinity on top and 20 vol% crystallinity on the bottom, and Sim. (4) with 10 vol% crystallinity on top and 10 vol% crystallinity on the bottom. We compare different snapshots of the simulations. The crystal fractionation is most efficient for Sim. (1) but the efficiency is comparable to Sims. (2–3) and (4) is the least efficient. Crystal-melt segregation speed is comparable for Sims.(1-3), but crystal-melt segregation speed on average is much lower for Sim. (4). However, segregation speed for Sim. (4) is faster than hindered settling. Cluster-melt segregation speed is comparable for (1–3).

With time, crystals in (2-3) lock up with other crystals, preventing advection of the crystals. Whereas crystals in (1) are able to freely settle through crystal-free melt. This is an explanation as to why the clusters in (2-3) experience less and slower crystal fractionation. Cluster formation still occurs in (4), making it faster than hindered settling would have suggested; however removing the gradient significantly slows down the speed of crystal-melt segregation and hence crystal fractionation.

6 Variability in crystal population

The flow fields that result from cluster settling are unlikely to be preserved in erupted lava because the transport from magma processing zone to volcano conduit will disrupt the collective motion that defines the clusters. Also, because cluster settling is a process unique to liquid-rich regions, the transition from melt-rich to crystal-rich systems could overprint the clusters. Therefore, it is unlikely for clusters to be preserved in plutonic bodies. However, the crystal population in igneous rock samples may preserve indirect signatures of cluster settling. We show one analysis in

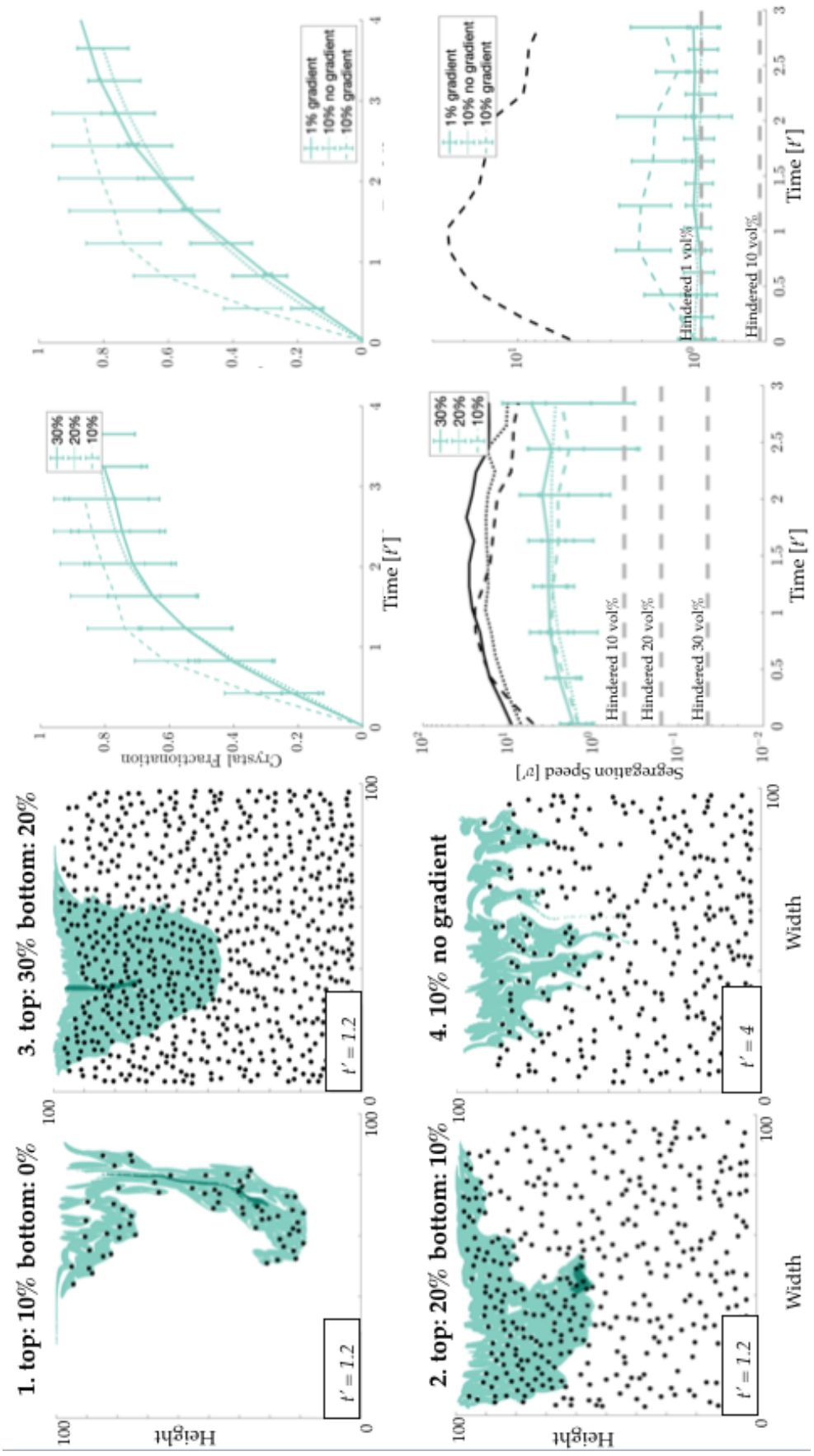

Figure 5. Simulation runs testing efficiency. The figure is set up to mimic Fig. 2 in the Manuscript. Simulations 1–3 have a gradient in crystallinity of 10 vol%. Simulation 1 is the same as the simulation in Fig. 2 of the Manuscript. We show the segregation speeds and crystal fractionation rates Γ. We only show cluster-melt segregation speed for Simulation 1–3, because Simulation 4 does not form a single large cluster. Additionally, for figure simplicity, we do not show the individual crystal-melt segregation and crystal fractionation in dark turquoise.

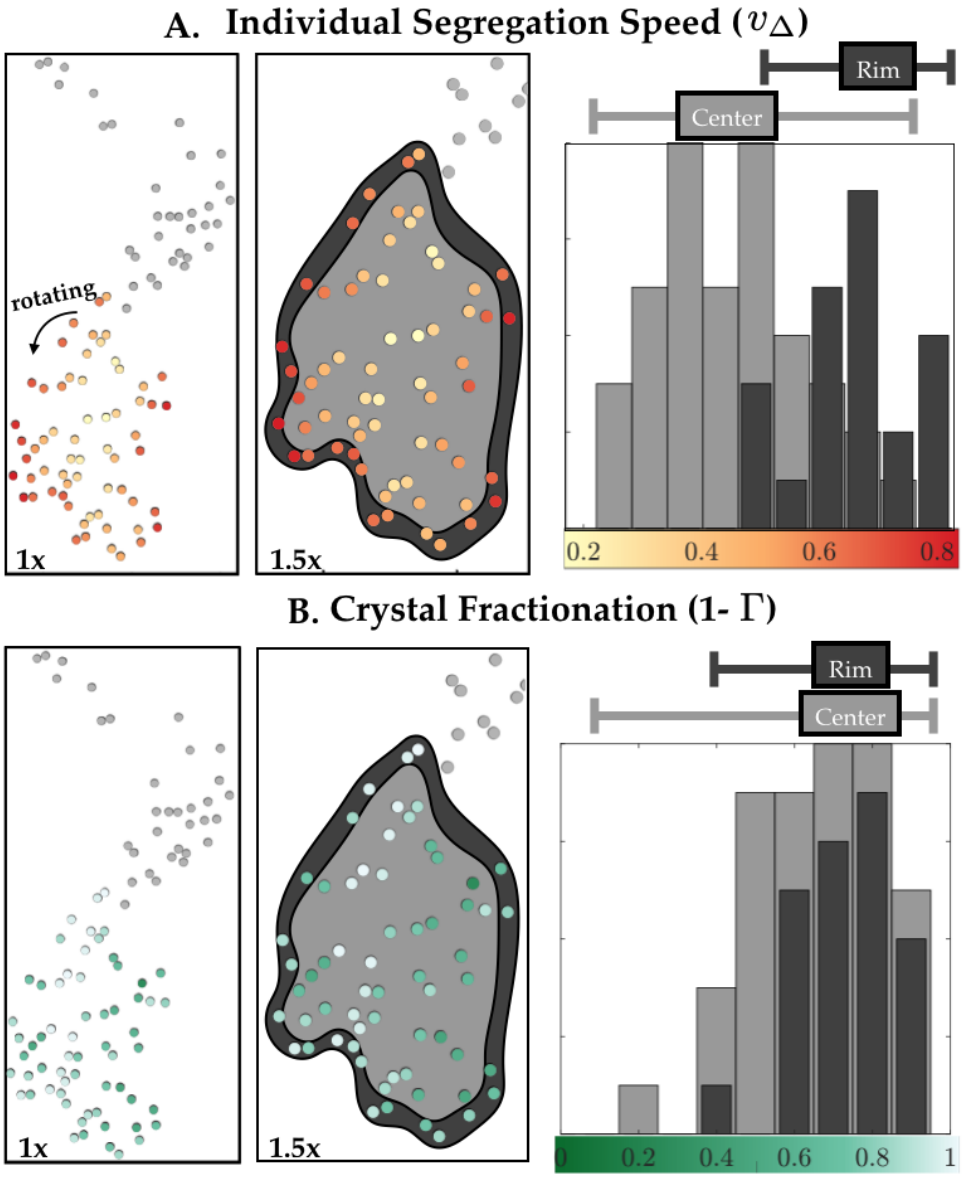

Figure 6. Explaining the observational signatures of convection driven fractionation. Individual crystal segregation speed is shown in (A) and individual crystal fractionation is shown in (B). Figures on the left show a simulation with 10 vol% crystallinity at a single point in time. Individual crystals are colored yellow (slow) to red (fast) to indicate the degree of crystal segregation speeds and dark (no crystal fractionation) to light (full crystal fractionation) green to indicate the degree of crystal fractionation. Dark gray crystals are part of the simulation but are not included in the calculation. The middle figures show which crystals were hand selected to fall in the rim (dark gray) and in the cluster center (light gray). The histograms in the right indicate the distribution of these metrics at either crystal center or crystal rim.

the Manuscript that has direct connection to natural data set. Here we will explore another example that still needs to be connected to natural data set.

We observe that each crystal in a collectively settling cluster segregates and thus fractionates at a different rate depending on its location between the cluster center and rim. We manually identify the crystals that are inside the cluster (light gray) and along the cluster rim (dark gray) in Supp. Fig. 6. On average, the crystals on the rim show higher crystal segregation speeds compared to crystals within the cluster (Supp. Fig. 6A). However, the degree of crystal fractionation is highly variable throughout the cluster (Supp. Fig. 6B).

The degree of crystal fractionation at any given time is a snapshot of the crystal's integrated segregation history. For example, the highlighted red crystal in the 10 vol% crystallinity simulation shown in the Manuscript Fig. 2D-F travels through the cluster neck to the cluster center and finally to the cluster rim. Along this trajectory, its crystal segregation speed is initially higher than the average segregation speed, before slowing down to values similar to the individual settling speed, and finally ending up faster than the average speed again. Each of the crystals continuously shift position relative to one another in the cluster. Clusters are hence dynamically evolving structures. This dynamic evolution allows crystals that formed in opposite ends of the domain to reside next to one another. Examples of olivine crystals with different compositions next to one another could be an example of this subtle variability (e.g., Wieser et al., 2019).

Our results suggest that static clusters would preserve a crystal fractionation population that is similar to the histogram in Fig. 6A, two distinct distributions, whereas dynamic clusters would preserve Fig. 6B. Although growth, dissolution, and nucleation properties of crystals are difficult to model, we hypothesize that histograms of crystalline populations at idealized regions–such as the thick flood-basalts (e.g., Cornwall, 1951; Greenough & Dostal, 1992; Puffer & Horter, 1993) containing horizontal layers of magma that have experienced fractional crystallization post eruption–could determine how dynamic clusters are in magmatic units. This would allow us to better characterize the ideal properties of quickly fractionating magma.

6.1 Quantifying disequilibrium

A relatively low segregation speed between a given crystal and the surrounding melt suggests that the crystal interacts with it for longer than the average crystal interacts with its surrounding melt. This prolonged interaction could translate to an increase in degree of chemical equilibration with the surrounding melt. Since each crystal takes a different path within the cluster, crystals that might come to rest next to each other might show different degrees of chemical interaction with surrounding melt. Generally, the crystals in a cluster will record greater heterogeneity than individual settling crystals. This heterogeneity might be recorded in hand samples as subtle variability in crystal sizes or geochemistry.

At the crystalline scale, the degree of equilibration of crystals with the nearby melt during settling can be characterized by the non-dimensional ratio $D_c/(v_\Delta a)$, a function of the chemical diffusivity, D_c, crystal segregation speed, v_Δ, and crystal size, a. If the segregation speed is large relative to the chemical diffusion rate, the crystal will remain in geochemical disequilibrium. At the mesoscale, since the cluster rims are chemically isolating the cluster center, the cluster rim is most prone to disequilibrium. The crystal-melt segregation speed of crystals in the cluster rim approach V_Δ. Therefore, $D_c/(V_\Delta a)$ would approximate the maximum degree of disequilibration of crystals in crystal-driven convection.

References

Cornwall, H. R. (1951). Differentiation in lavas ofthe Keweenawan series and the origin ofthe copper deposits of Michigan. *J. Chem. Inf. Model.*, *62*, 159—-202. doi: 10.1017/CBO9781107415324.004

Greenough, J. D., & Dostal, J. (1992). Layered rhyolite bands in a thick North Mountain Basalt flow: the products of silicate liquid immiscibility? *Mineral. Mag.*, *56*(384), 309–318. doi: 10.1180/minmag.1992.056.384.02

Michioka, H., & Sumita, I. (2005). Rayleigh-Taylor instability of a particle packed viscous fluid: Implications for a solidifying magma. *Geophys. Res. Lett.*, *32*(3), 1–4. doi: 10.1029/2004GL021827

Puffer, J. H., & Horter, D. L. (1993). Origin of pegmatitic segregation veins within flood basalts. *Geol. Soc. Am. Bull.*, *105*(6), 738–748. doi: 10.1130/0016-7606(1993)105⟨0738:OOPSVW⟩2.3.CO;2

Qin, Z., Alison, K., & Suckale, J. (2019). Rotation matters-direct numerical simulations of rectangular particles in suspensions at low to intermediate solid fraction. *arXiv preprint arXiv:1903.08167*.

Qin, Z., & Suckale, J. (2017). Direct numerical simulations of gassolidliquid interactions in dilute fluids. *Int. J. Multiph. Flow*, *96*(November), 34–47.

Rayleigh, L. (1883). Investigation of the Character of the Equilibrium of an Incompressible Heavy Fluid of Variable Density. *Proc. London Math. Soc.*, *14*(39), 170–177.

Sir Geoffrey (F.R.S.), T. (1950). The Instability of Liquid Surfaces when Accelerated in a Direction Perpendicular to their Planes. II. *Proc. R. Soc. A Math. Phys. Eng. Sci.*, *202*(1068), 81–96. Retrieved from `http://rspa.royalsocietypublishing.org/cgi/doi/10.1098/rspa.1950.0086` doi: 10.1098/rspa.1950.0086

Wieser, P. E., Vukmanovic, Z., Kilian, R., Ringe, E., Holness, M. B., Maclennan, J., & Edmonds, M. (2019). To sink, swim, twin, or nucleate: A critical appraisal of crystal aggregation processes. *Geology*, *47*(10), 948–952. doi: 10.1130/g46660.1